Current Applied Physics 56 (2023) 16–23

Contents lists available at ScienceDirect

Current Applied Physics

journal homepage: www.elsevier.com/locate/cap

Theoretical proposal of a sensor based on the comb-shaped coherent absorption realized by the magnetized plasma photonic crystals

Fu-Pei Wu, Jia-Tao Zhang, Hai-Feng Zhang *

College of Electronic and Optical Engineering & College of Flexible Electronics (Future Technology), Nanjing University of Posts and Telecommunications, Jiangsu province, 210023, China

A R T I C L E I N F O

Keywords:
Coherent perfect absorption
Sensor
Plasma photonic crystals
Multiphysical quantities measurement
Characteristic matrix method

A B S T R A C T

The study presents a theoretical framework outlining a sensor capable of realizing comb-shaped coherent absorption peaks in magnetized plasma photonic crystals. The proposed model enables simultaneous measurement of alterations in the applied magnetic induction intensity, thickness of the dielectric layer, incident angle of electromagnetic waves, and the refractive index. The nascent stage of coherent absorption theory's application to photonic crystals is currently under scrutiny. Enabling interaction between both forward and backward propagating electromagnetic waves at either end of the photonic crystals creates comb-shaped absorption peaks for detecting variances in physical quantities. The sensor model utilized the transfer matrix method for computation of the transmission and reflection coefficients, linear range, sensitivity, and further linear fitting equations across all physical quantities when employed for multi-physics measurements. The present study entailed an analysis of linear range, the figure of merit, and the sensitivity of a sensor designed to detect magnetic induction intensity. Results demonstrate that the linear range from 0.7 T–1.3 T, while the figure of merit equals 50.2189 T^{-1} and sensitivity equals 4.3535 × 10-8 (ωd/2πc)/T. Conversely, when measuring thickness, the corresponding linear range extends from 0.4–0.85 mm, with figure of merit reaching 481.06 mm^{-1} and sensitivity equating to 3.5567 × 10-4 (ωd/2πc)/mm. Additionally, the sensor's application to the measurement of both incident angle and refractive index revealed parameters for linear range that ranged from 2 to 4.1, while figure of merit was calculated at 124.00 RIU^{-1} and sensitivity at 15.54952 (ωd/2πc)/RIU. Regarding incident angle, related values for linear range spanned from 15°–44°, with figure of merit established at $4.2157^{\circ -1}$ and sensitivity at 0.8661 (ωd/2πc)/degree.

1. Introduction

Photonic crystals (PCs) represent a layered and periodic structure composed of materials with different refractive indices. Since their discovery, researchers have been drawn to them for the distinctive optical characteristics they impart [1,2]. The propagation of electromagnetic (EM) waves through PCs has been observed to manifest analogous features to that of electrons moving through semiconductor materials. Specifically, forbidden bands, known as photonic band gaps, emerge, impeding the passage of EM waves [3,4]. The introduction of plasma as a lossy medium to the layered structure of PCs provides an exceptional optical response, as evidenced by the development of comb-shaped absorption peaks with a tunable number and substantial absorption intensity in this investigation. Furthermore, since the frequency band of the absorption peaks with comb-shaped morphology is adjustable through the plasma cyclotron frequency, which represents the strength of the external magnetic field, the absorption peaks' comb-shaped formation may be employed as a probe for sensing the magnitude of external magnetic induction [5–7]. Most studies analyzing magnetized plasma photonic crystals (MPPCs) concentrate on their optical response when exposed to electromagnetic waves propagating unidirectionally. Regarding this, adjustments such as changes in the thickness of the plasma layer, the plasma frequency, and the electron collision frequency can be implemented, ultimately affecting plasma absorption behavior [8]. Nevertheless, this present inquiry implements an approach that entails the utilization of forward and backward propagating electromagnetic waves that are induced at each end of the complete PCs structure [9,10].

In 2011, Longhi et al. explored the time-reversed laser process in a two-energy medium with uniform widening in the optical cavity and

* Corresponding author.
E-mail address: hanlor@163.com (H.-F. Zhang).

https://doi.org/10.1016/j.cap.2023.09.006
Received 17 April 2023; Received in revised form 27 August 2023; Accepted 18 September 2023
Available online 26 September 2023

Table 1
Comparison of optimal parameters for each sensor.

Reference	Physical quantity	LR	S	FOM	Physical mechanism
[23]	Magnetic field	1.9 T–2.55 T	0.838 THz/T	34.2 T^{-1}	Evanescent wave
	Thickness	None	None	None	
	Incidence angle	None	None	None	
	Refractive index	1.4–3.8	7.144 THz/RIU	5656.7 RIU^{-1}	
[24]	Magnetic field	None	None	None	Multimodal interference
	Thickness	None	None	None	
	Incidence angle	None	None	None	
	Refractive index	1∼3.5	1.58 THz/RIU	3.6 × 105 RIU^{-1}	
[25]	Magnetic field	0.2 T–2.6 T	1.41 GHz/T	30.65 T^{-1}	Defect mode resonance
	Thickness	None	None	None	
	Incidence angle	28°∼78°	0.98 GHz/degree	24.75$^{\circ -1}$	
	Refractive index	1.05–2.05	34.3 GHz/RIU	634 RIU^{-1}	
This work	Magnetic field	0.35 T–0.65 T	3.716 GHz/T	50.16 T^{-1}	CPA
	Thickness	0.8 mm–1.70 mm	27.174 GHz/mm	312.44 mm^{-1}	
	Incidence angle	15°∼44°	0.216 GHz/degree	2.97$^{\circ -1}$	
	Refractive index	2∼4.1	124.00 GHz/RIU	74.55 RIU^{-1}	

further advanced the determination of conditions for the coherent perfect absorption (CPA) [11]. The findings indicate that the frequency of the CPA generation field generally differs from the laser mode because of the two-energy medium's dispersion characteristic, which results in a breach of the exact time-reversal symmetry. As a consequence, EM waves satisfying coherence requirements will interfere, allowing for the two oppositely propagating beams to be absorbed coherently. It is noteworthy that variations in the phase difference between the forward and backward incident EM waves can be utilized to regulate the amplitude of CPA. Specifically, as the phase difference shifts from 0 to π, the amplitude of CPA can be modulated to range between 0 and 1 [12–16]. Previously, producing narrow-band CPA in a 100 μm-thick silicon film [17] or single-wavelength CPA in plasma [18] involved establishing a fixed phase relationship between two laser beams. However, in 2017, Pye et al. demonstrated the generation of coherent perfect absorption with a noncoherent beam of light at all resonances in a 2 μm thick polycrystalline silicon film having a flat spectrum via the use of a thin, nonperiodic dielectric mirror [19]. Moreover, achieving coherent perfect absorption is possible by employing photonic doping in zero-index media with absorptive defects [20], and incorporating ultrathin conductive films in the medium provides a means towards attaining geometrically invariant multichannel coherent perfect absorption [21]. In 2021, Wu et al. introduced the concept of coherent absorption (A_c) in one-dimensional (1-D) plasma PCs and demonstrated that A_c appears at specific frequency points with the absorption amplitude modulated by the initial phase, enabling control over values ranging from 0.9994 to 0.1122 [22]. Based on this study, by magnetizing the plasma layer and redesigning the PCs construction, an unprecedented cluster of comb-shaped A_c peaks was achieved.

Furthermore, in 2021, Rao et al. developed a novel sensor utilizing magnetized ferrite PCs capable of measuring refractive index and magnetic induction intensity in both forward and backward scales [23]. As depicted in Table 1, the innovative design principle adopted in this study enables the measurement of multiple physical quantities while maintaining excellent performance parameters. In 2020, Zaky et al. developed a refractive index gas sensor utilizing 1-D PCs with a measurement linear range (LR) of 13.5 and a sensitivity (S) of up to 1.58 THz/RIU based on the optical Tamm state (OTS), an interfacial mode inspired by the Tamm analogy in solid-state physics that demonstrates enhanced field localization at partition interfaces of dissimilar materials [24]. Additionally, in 2021, Wan et al. designed a novel multi-physics quantity sensor utilizing 1-D plasma PCs, achieving an LR of 28°–78° and an S of 0.98 THz/degree when measuring the angle of incidence, and an LR of 1.05–2.05 and an S of 34.3 THz/RIU when measuring the refractive index [25]. The present sensor design proposes measurement of the angle of incidence and refractive index, achieving the LR of 15°–44° and the S of 0.2161 GHz/degree for the former, and the LR of 2∼4.2 and the S of 5.4146 GHz/RIU for the latter. In 2022, Panda et al. designed a tunable filter with channel using two dielectric materials and magnetized cold plasma. They utilized the transfer matrix method to calculate the effect of magnetic field on the filter frequency and evaluated the performance of the filter through different geometric parameters [26]. In the same year, Zaky et al. designed a novel magnetic field-dependent sensor using cold plasma. The calculation results demonstrated a close correlation between the defect mode frequency and the refractive index of the sample. The optimized sensor exhibited high sensitivity (15.14 GHz/RIU), quality factor (527.32), and advantageous parameters (1066.20 RIU−1) [27]. The studied sensor exhibits a narrower interval for angle measurements and a wider LR for refractive index measurements, as documented in Table 1.

This paper explores the sensing potential of the frequency band containing the comb-shaped A_c peak for measuring the external magnetic induction strength, dielectric layer thickness, angle of incidence of EM waves, and refractive index changes. As indicated in Table 1, the innovative physical model presented in this study surpasses conventional sensors by achieving versatile multi-physics measurements and incorporating coherent absorption theory in sensor design. In comparison to Ref. [23], the sensor presented in this study displays a superior figure of merit (FOM) for measuring magnetic intensity, but a markedly

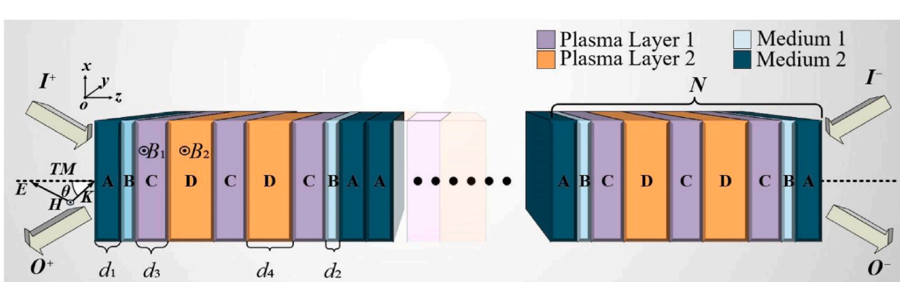

Fig. 1. Schematic diagram of 1-D MPPCs with bidirectional oblique incidence of EM waves.

inferior FOM in the measurement of refractive index, where FOM=S/FWHM, and FWHM denotes the full width at half maximum. The design of the structure ensures that the relative bandwidth of absorption peaks remains minimally impacted when measuring distinct physical parameters. Accordingly, a direct correlation is observed between FOM and sensitivity in measuring individual physical quantities. Since the research presented in this paper is rooted in the CPA theory, adherence to the coherence condition is imperative for determining the phase difference between forward and backward incident EM waves (i.e. the phase difference must be 0 or π). Consequently, limitations are imposed on LR, S, and FOM, in order to enable accurate measurements of certain physical quantities. A noteworthy aspect of this work, in comparison to Ref. [24], is the significantly increased number of measurements conducted, which exhibit superior performance parameters. Further, better LR, higher S, and different angle measurement LR are observed when measuring the refractive index relative to Ref. [25]. In future studies, we will prioritize improving performance parameters as our primary research goal.

2. Theoretical model and formulations

In Fig. 1, the MPPCs are irradiated by two EM waves in opposite directions, and the two EM beams satisfying the coherence condition interfere with each other throughout the sensor model, and A_c occurs.

$$\boldsymbol{M}_{pC,D}=\begin{pmatrix}\cos\left(k^x_{C,D}d_{3,4}\right)+\frac{k^z_{C,D}\varepsilon_2}{k^x_{C,D}\varepsilon_1}\sin\left(k^x_{C,D}d_{3,4}\right) & -\frac{i}{\eta_{C,D}}\left[1+\left(\frac{k^z_{C,D}\varepsilon_2}{k^x_{C,D}\varepsilon_1}\right)^2\right]\sin\left(k^x_{C,D}d_{3,4}\right)\\ -i\eta_{C,D}\sin\left(k^x_{C,D}d_{3,4}\right) & \cos\left(k^x_{C,D}d_{3,4}\right)-\frac{k^z_{C,D}\varepsilon_2}{k^x_{C,D}\varepsilon_1}\sin\left(k^x_{C,D}d_{3,4}\right)\end{pmatrix}, \tag{5}$$

The sensor model is arranged periodically along the z-direction, with N = "ABCDCDCBA" as a repeating unit. A with thickness $d_1 = 0.022$d, d = $2\pi c/\omega_p$ is the normalization constant [29], where the definition of the plasma frequency (ω_p) we give in the subsequent discussion, and c is the speed of light in a vacuum, and B with thickness $d_2 = 0.005$d in this sensor represent two different normal isotropy and lossless dielectrics with dielectric constants $\varepsilon_A = 2.1$, $\varepsilon_B = 9.8$, respectively. C and D denote the magnetized plasma layers with thicknesses $d_3 = 0.063$d, $d_4 = 0.08$d, and applied magnetic induction strengths B_1 and B_2, respectively. Under the TM mode, the forward and backward EM waves incident at an angle of incidence of θ are denoted by I^+, I^-, respectively, and O^+, O^- represent the output EM waves after passing through the whole sensor.

Due to the various anisotropies of the plasma, the dielectric constant in the presence of an applied magnetic field has the following form [28]:

$$\boldsymbol{\varepsilon}=\begin{pmatrix}\varepsilon_1 & 0 & i\varepsilon_2\\ 0 & \varepsilon_3 & 0\\ -i\varepsilon_2 & 0 & \varepsilon_1\end{pmatrix}, \tag{1}$$

where

$$\varepsilon_1=1-\frac{\omega_p^2(\omega+i\nu)}{\omega\left[(\omega+i\nu)^2-\omega_c^2\right]},\ \varepsilon_2=\frac{-\omega_p^2\omega_c}{\omega\left[(\omega+i\nu)^2-\omega_c^2\right]},\ \varepsilon_3=1-\frac{\omega_p^2}{\omega(\omega+i\nu)}.$$

The frequency of the incident wave is expressed by ω. ω_p, ν, and ω_c=qB/m$_0$ are the plasma frequency, collision frequency, and cyclotron frequency, respectively. Where $\omega_p=q^2n_e/(\varepsilon_0 m_0)$, $n_e = 10^{18}$ m^{-3} is the plasma density, $q=1.6\times10^{-19}$ C and $m_0 = 9.1\times10^{-31}$ kg are the charge and mass of the electron, respectively, $\varepsilon_0 = 8.8542\times10^{-12}$ F/m is the dielectric constant under vacuum, $\omega_{c1} = 2.4\omega_p$ of plasma layer C, and $\omega_{c2} = 5\omega_p$ of plasma layer D. In TM mode, the effective dielectric function can be indicated as [28,29].

$$\varepsilon_{eff}=\frac{\varepsilon_1^2-\varepsilon_2^2}{\varepsilon_1}. \tag{2}$$

Calculation of the action of PCs on incident waves using the characteristic matrix method

$$\mathrm{M}=\left(\mathrm{M_A M_B M_{\mathit{p}C} M_{\mathit{p}D} M_{\mathit{p}C} M_{\mathit{p}D} M_{\mathit{p}C} M_B M_A}\right)^L=\begin{vmatrix}M_{11} & M_{12}\\ M_{21} & M_{22}\end{vmatrix}. \tag{3}$$

For dielectrics A and B, the transmission matrix is shown below [29].

$$\boldsymbol{M}_{A,B}=\begin{pmatrix}\cos\delta_{A,B} & -\frac{i}{\eta_{A,B}}\sin\delta_{A,B}\\ -i\eta_{A,B}\sin\delta_{A,B} & \cos\delta_{A,B}\end{pmatrix}, \tag{4}$$

where $\delta_{A,B}=(2\pi/\lambda)d_{1,2}\cos\theta_{A,B}n_{A,B}$, $\theta_{A,B} = \arcsin(n_0\sin\theta/n_{A,B})$, $\eta_{A,B}=(\varepsilon_0/\mu_0)^{1/2}n_{A,B}/\cos\theta_{A,B}$, where $n_{A,B}=\varepsilon_{A,B}^{1/2}$, $d_{1,2}$, $\theta_{A,B}$ are the refractive index, the thickness of A, B and incident angle of the layer, respectively. $n_0 = 1$, $\theta=0°$ is the refractive index and the incident angle of air, $\mu_0 = 4\pi\times10^{-7}$ N/m is the vacuum permeability. L=16 means the number of minimum periodic cells.

For a magnetized plasma layer, its transport matrix can be formulated as [29].

where $\eta_{C,D}=(\varepsilon_0\varepsilon_{eff}/\mu_0)^{1/2}n_{C,D}/\cos\theta_{C,D}$, $k^x_{C,D} = k_{C,D}\cos\theta_{C,D}$, $k^z_{C,D} = k_{C,D}\sin\theta_{C,D}$, $k_{C,D}=(\varepsilon_{eff}\omega^2/c^2)^{1/2}$.

The reflection (r) and transmission (t) coefficients have the following forms

$$r=\frac{(M_{11}+M_{12}\eta_0)\eta_0-(M_{21}+M_{22}\eta_0)}{(M_{11}+M_{12}\eta_0)\eta_0+(M_{21}+M_{22}\eta_0)},\quad t=\frac{2\eta_0}{(M_{11}+M_{12}\eta_0)\eta_0+(M_{21}+M_{22}\eta_0)} \tag{6}$$

where $\eta_0=(\varepsilon_0/\mu_0)^{1/2}/\cos\theta$, therefore, the corresponding reflectance (R), transmittance (T), and material intrinsic absorptance (A_b) are

$$R=|r|^2, \tag{7}$$

$$T=|t|^2, \tag{8}$$

$$A_b=1-R-T. \tag{9}$$

We generalize the relationship between the incident (I^+, I^-) and output (O^+, O^-) EM waves at both ends through the scattering matrix $\boldsymbol{S}$ as [30]:

$$\begin{bmatrix}O^+\\ O^-\end{bmatrix}=\boldsymbol{S}\begin{bmatrix}I^+\\ I^-\end{bmatrix}=\begin{bmatrix}t^- & r^+\\ r^- & t^+\end{bmatrix}\begin{bmatrix}I^+\\ I^-\end{bmatrix}, \tag{10}$$

if in the symmetric system, $t^+=t=t^-$, $r^+=r=r^-$, the above equation can be written as:

$$O^+=tI^++rI^-,\quad O^-=rI^++tI^- \tag{11}$$

A_c in the whole sensor is expressed as [30]:

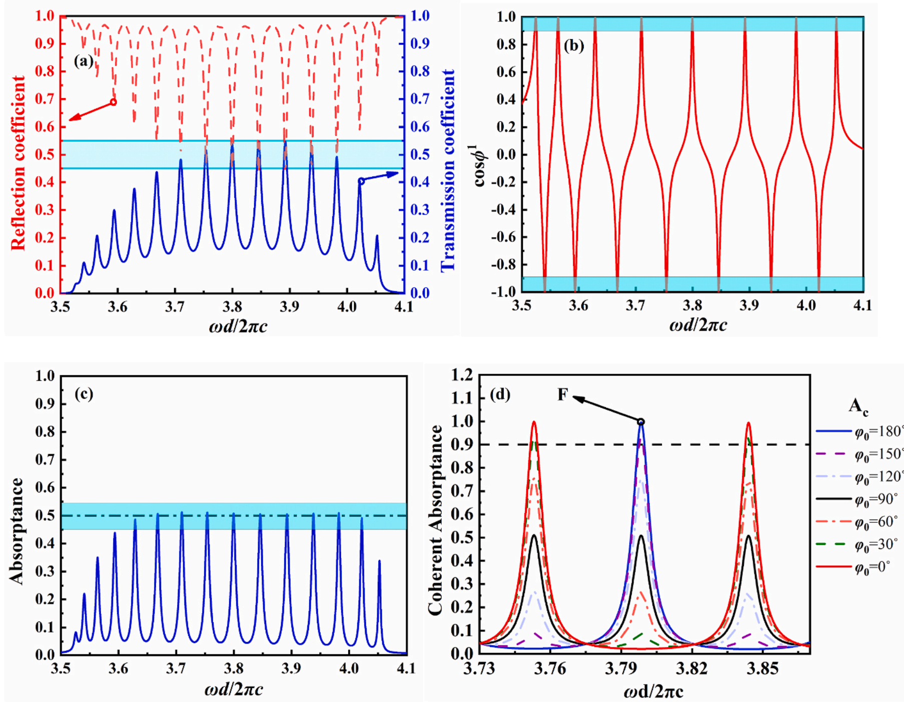

Fig. 2. When L = 16, θ=0°, the criteria necessary to provide CPA and the phase modulation properties. (a) The relation between the amplitude of t of a forward transmitted EM wave and r of a backward propagating wave in a coherent band. (b) The coherent condition is satisfied when cos$\Delta\varphi_1$ is equal to 1 or -1. (c) A_b of sensor models. (d) Change in the amplitude of CPA when φ_0 varies from 1 to 2.

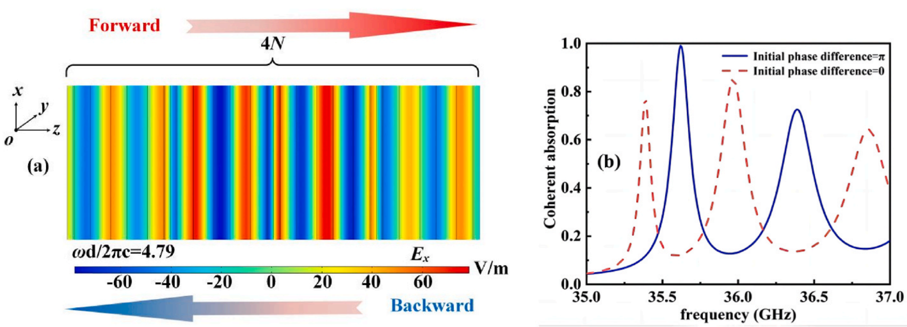

Fig. 3. (a)When L = 4, the electric field intensity distribution along the z-direction at the frequency point where A_c occurs is plotted. (b) A_c is regulated by initial phase difference.

$$A_c = 1 - \frac{|O^+|^2 + |O^-|^2}{|I^+|^2 + |I^-|^2} = 1 - (|t| - |r|)^2 - 2|tr|\left(1 + \cos\Delta\varphi_1 \cos\varphi_0 \frac{2|I^+||I^-|}{|I^+|^2 + |I^-|^2}\right), \tag{12}$$

where $\Delta\varphi_1$ and φ_0 are the phase difference between the r and t, and the incident waves, respectively. When the above equation satisfies the condition:

$$\begin{aligned} & t = \pm r \\ & \cos\Delta\varphi_1 \cos\varphi_0 = -1, \\ & |I^+| = |I^-| \end{aligned} \tag{13}$$

A_c has a maximum value.

3. Results and discussions

With a guarantee of equal incident wave amplitude $|I^+| = |I^-|$ and calculation results that align with the aforementioned A_c condition, a comb-shaped peak at frequency points that align with the coherence condition is exhibited, showcasing the absorption as represented in Fig. 2(d). Notably, as shown in Fig. 2(a) and (b), the sum of the final two terms of the A_c equation is minimal when the amplitudes of t are roughly equal to r, both of which equal 0.5, and $\cos\Delta\varphi_1\cos\varphi_0 = -1$, resulting in A_c taking a value of 1. Comparing Fig. 2(c) with Fig. 2(d), it is apparent that the implementation of the CPA theory enables a significant hike in the original absorption amplitude from 0.5 to 1. Theoretical derivations highlight that the amplitude of A_c is further modulated by the phase difference of the incident wave, in a manner that regulates absorption from 0 to 1. As seen in Fig. 2(d), the two notable absorption maxima experienced beyond the 0.9 thresholds represent absorption profiles at the phase difference values of either 0 or π, both of which can be regulated to modulate A_c at corresponding frequency points in the range 0~1 through the modification of φ_0. The modulation of φ_0 at 60° or 120° gives rise to a notable drop in the amplitude of A_c, from the original value of 0.9984 to 0.7544, recorded across different frequency points. Conversely, when φ_0 is set at 90°, the coherent absorption phenomenon ceases to exist, with only the intrinsic absorption peak featuring an

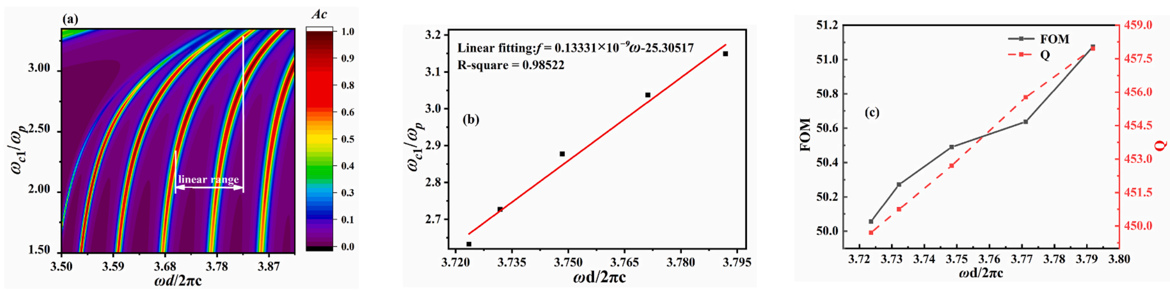

Fig. 4. (a) The three-dimensional (3-D) plan view of the comb-shaped A_c peaks with magnetic intensity changes. (b) The linear fitting equation between magnetic induction intensity and frequency. (c)The Q and FOM variation with frequency.

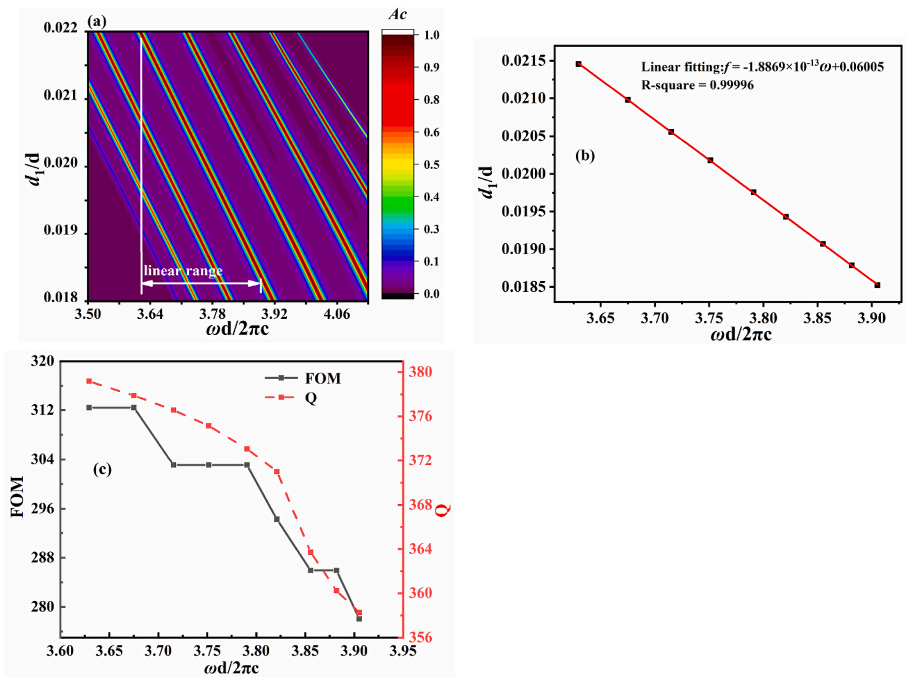

Fig. 5. (a)The 3-D plan view of the comb-shaped A_c peaks with thickness of dielectric changes. (b) The linear fitting equation between thickness of dielectric and frequency. (c) The Q and FOM variation with frequency.

amplitude of 0.5104 in place. Additionally, since the absorption peak at F is positioned at the center and displays a Q value of 445.90, the measurement is strategically placed at $\omega = 3.80\alpha$, where $\alpha = 2\pi c/d$.

Fig. 3(a) provides a visual representation of the distribution of electric field energy at the specified frequency point $\omega = 4.79\alpha$, which satisfies the coherent absorption condition for $L = 4$. The planned structural unit displays periodic fluctuations in electric field energy when arranged periodically, with an amplitude that ranges from a minimum of −65 V/m to a maximum of 65 V/m across the center of the structure. In general, the distribution of energy in the electric field is uniform and of a low amplitude, concentrated between −15 V/m and +15 V/m around the periphery of the sensor. However, periodic changes in the energy state with high intensity are observed, indicating the interaction between two counter-propagating light beams and demonstrating the good electromagnetic absorption properties of the sensor. Fig. 3(b) illustrates the feasibility of the comb-shaped coherent absorption effect realized in the sensor, as confirmed by the results obtained from the computational Fig. 1 modeling conducted in the finite difference time domain (FDTD) method. Specifically, a comb-shaped A_c peak is detected within the predicted band range, where the absorption amplitude and position are found to be modulated by diverse initial phases. Nevertheless, it is important to note that the material losses and mesh dissection inherent in the FDTD simulation can give rise to discrepancies from the expected theoretical calculations.

Initially, the sensor can be utilized for magnetic induction strength characterization. This is exemplified in Fig. 4(a) where the position of A_c peaks is denoted as the magnetic induction strength varies. In particular, measurement results demonstrate that a majority of absorption peaks in the LR region hold amplitudes above 0.9, with the maximum reaching 0.9953. It is important to note that the magnetic induction intensity varies between 0.7 T and 1.3 T, whilst retaining good linearity with coherent frequency points, ultimately A_c amplitude larger than 0.9. The specific data analysis is presented in Fig. 4(b) which exhibits the linear fitting equation of frequency-magnetic induction within the range of $\omega = 3.72\alpha \sim \omega = 3.79\alpha$, where $f = 0.13331 \times 10^{-9}\omega$-25.30517. By converting to 4.3535×10^{-8} ($\omega d/2\pi c$)/T, the S can be derived. The R-square value associated with this linear equation is 0.98522, which confirms the linearity requirements for the sensor's design. Additionally, the FOM, with Q = 449.71, is calculated to be 50.16 T^{-1} when B_1 equals 0.9 T and ω equals 3.72α. In consideration of Fig. 4(c), a slight increase in the values of FOM and Q is observed as the frequency increases. At the specific frequency point of $\omega = 3.72\alpha$, the values of FOM and Q are calculated to be 50.16 T^{-1} and 449.71, respectively. Moreover, at the frequency point of $\omega = 3.79\alpha$, its values escalate to 51.06 T^{-1} and

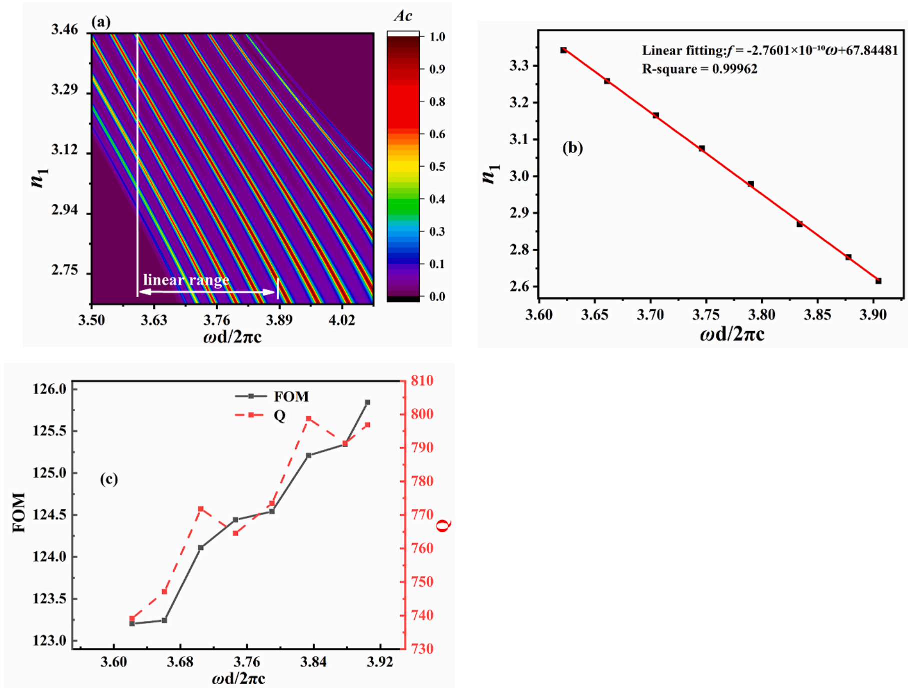

Fig. 6. (a) The 3-D plan view of the comb-shaped A_c peaks with refractive index changes. (b) The linear fitting equation between refractive index of dielectric and frequency. (c) The Q and FOM variation with frequency.

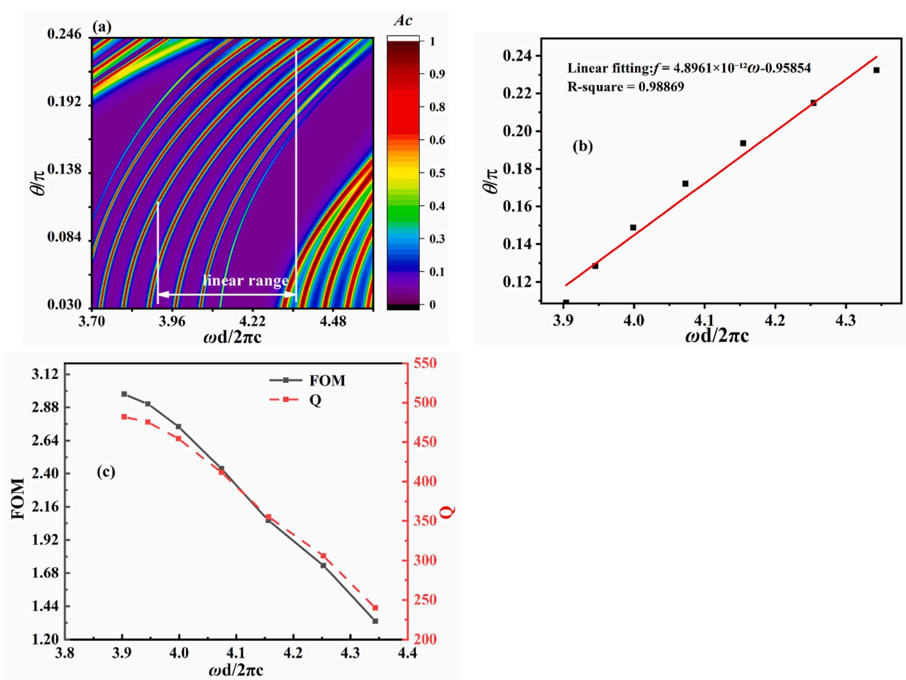

Fig. 7. (a) 3-D plan view of the comb-shaped Ac peaks with incident angle changes. (b) The linear fitting equation incident angle and frequency. (c) The Q and FOM variation with frequency.

457.96. The applied magnetic field solely affects the plasma layer, thus it is crucial that the plasma layer is set as the sensitive area during magnetic induction intensity measurements.

Furthermore, the proposed sensor demonstrates the capability of measuring the dielectric layer's thickness. Interestingly, the superior S and LR of the sensor are evident when utilized with media A and B. Owing to space constraints, media A was chosen for detailed investigation. As illustrated in the 3-D plot in Fig. 5(a), a significant number of A_c peaks have an amplitude surpassing 0.9, and there is no observable decay in amplitude fluctuations due to thickness changes. Remarkably, the sensor possesses an absorption value up to 0.9990, further affirming its potential for precision measurement of dielectric layer thickness. The obtained linear fitting equation depicting the relationship between frequency and thickness is demonstrated in Fig. 5(b). Within the range of $\omega = 3.60\alpha$ to $\omega = 3.92\alpha$ and a corresponding thickness of d = 67 mm, the LR of the thickness variation is observed to be approximately 0.8

mm–1.70 mm, which is expected to be wider. The equation is fitted as $f = -1.8869 \times 10^{-13}\omega+0.06005$. Notably, the high R-square value of 0.99996 indicates excellent linearity of the sensor in accordance with the set criteria. Subsequent calculations yielded the S and FOM of the thickness sensor as 3.5567×10^{-4} (ωd/2πc)/mm and 312.44 mm^{-1}, respectively, with Q = 374.19. Moreover, it is apparent from Fig. 5(c) that with increasing frequency, the FOM and Q values exhibit a gradual decrease from 312.44 mm^{-1}–278.04 mm^{-1} and 374.19 to 358.27, respectively. Nonetheless, this decline does not significantly impact the performance within the measurement range. Importantly, it is worth noting that the research on the PCs thickness sensor is still in its preliminary stages, and the implications of this work are anticipated to have a broad range of potential applications.

On the other hand, the sensor's efficacy is similarly exceptional when applied to gauge the refractive index of substance A. The positional shift of pattern A_c is depicted in Fig. 6(a), as the refractive index alters within the covered frequency range of $\omega = 3.62\alpha$ to $\omega = 3.92\alpha$. The majority of A_c peaks shown in the figure exhibit an absorption amplitude greater than 0.9, with no decline in amplitude despite the change in absorption peak position. Fig. 6(b) displays the linear fit curves for the refractive index and frequency. The refractive index exhibits linear variation between the ranges of 2 and 4.1. The highly linear fit curve depicted with an R-square value of 0.99962 is $f = -2.7601 \times 10^{-10}\omega+67.84481$, endorsing its potential for use in sensor design. Moreover, at a Q value of 739.16, the calculated S value of 15.54952 (ωd/2πc)/RIU and FOM of 123.20 RIU^{-1} suggest slightly inferior performance when contrasted with other sensors. However, it still meets the design criteria for achieving accurate measurements. Fig. 6(c) illustrates that the FOM value undergoes insubstantial variations as the frequency increases up to a maximum of 125.84. However, the Q undergoes an increase of 57.68, commencing from 739.16 and ending at 796.84.

Due to the limited availability of sensors for measuring incident angles, this paper presents the performance parameters when the absorber is utilized as an angle sensor. Fig. 7(a) presents a 3-D planar graph of the absorption peak position with respect to the angle. Notably, when the frequency transitions from $\omega = 3.91\alpha$ to $\omega = 4.35\alpha$, a favorable linear relationship between frequency and angle is established, ensuring a high absorption amplitude. The specific outcomes of the calculations are illustrated in Fig. 7(b). A high value of R-square = 0.98869, has been assured, and the linear fitting equation of $f = 4.8961 \times 10^{-12}\omega$-0.95854 has displayed a commendable linear relationship. Additionally, by computing the S of this angle sensor within the angle range of LR $14^\circ \sim 44^\circ$, it has been estimated to be 0.8661 (ωd/2πc)/degree, whereas the FOM under Q = 481.96 is measured to be $2.98^{\circ -1}$. Observations from Fig. 7(c) reveal that the frequency increase causes a decline in both the FOM and Q, though the reduction in FOM is insignificant. Specifically, the Q undergoes a decrease from 481.96 to 239.95, indicating a total decline of 242.01.

4. Conclusion

The study highlights the development of a physical model for MPPCs that underpins a sensor premised on comb-shaped coherence phenomena. This sensor enables the measurement of magnetic induction strength, dielectric thickness, refractive index, and incident angle, and can assess the performance of these four parameters. Additionally, enhancing the periodic constant's number can bolster Q and FOM values, thereby increasing absorption peaks. The major contribution of this research is in the application of CPA theory to multi-physics quantity measurements using a single sensor. This work has significant implications for pressure sensors, photosensitive sensors, and absorber design, and is expected to find widespread use in these areas.

Declaration of competing interest

We would like to submit the manuscript entitled "Theoretical proposal of a sensor based on the comb-shaped coherent absorption realized by the magnetized plasma photonic crystals", which we wish to be considered for publication in "Current Applied Physics". No conflict of interest exists in the submission of this manuscript, and the manuscript is approved by all authors for publication. I would like to declare on behalf of my co-authors that the work described was original research that has not been published previously, and not under consideration for publication elsewhere, in whole or in part. All the authors listed have approved the manuscript that is enclosed.

References

[1] E. Yablonovitch, Inhibited spontaneous emission in solid-state physics and Electronics, Phys. Rev. Lett. 58 (20) (1987) 2059–2062.
[2] H. Ma, B. Liang, S. Zhuang, J. Chen, Q. Jiang, J. Ding, Subwavelength imaging of a point source based on two-dimensional photonic crystals, Opt Lett. (2016) 3833–3835.
[3] A.H. Aly, D. Mohamed, M.A. Mohaseb, Theoretical and simulation study in defective semiconductor layer that incorporated with superconducting-dielectric photonic crystal, Int. J. Mod. Phys. B 33 (32) (2020).
[4] A.H. Aly, F.A. Sayed, THz cutoffff frequency and multifunction Ti2Ba2Ca2Cu3O10/GaAs photonic bandgap materials, Int. J. Mod. Phys. B 34 (10) (Feb, 2020) 30462.
[5] A. Chiasera, F. Scotognella, L. Criante, S. Varas, G.D. Valle, R. Ramponi, M. Ferrari, Disorder in photonic structures induced by random layer thickness, Sci. Adv. Mater. 7 (6) (May, 2015) 1207–1212.
[6] H. Hojo, K. Akimoto, A. Mase, Conference Digest on the 28th International Conference on Infrared and Millimeter Waves, 2003, pp. 347–348. Otsu, Japan.
[7] L. Qi, Z. Yang, Modified plane wave method analysis of dielectric plasma photonic crystal, Prog. Electromagn 91 (2009) 319–332.
[8] H.F. Zhang, M. Liu, Study of periodic band gap structure of the magnetized plasma photonic crystals, Optoelectron. Lett. 5 (2009) 112.
[9] Y.D. Chong, G. Li, C. Hui, A.D. Stone, Coherent perfect absorbers: time-reversed lasers, Phys. Rev. Lett. 105 (5) (2010), 53901.
[10] W. Wan, Y.D. Chong, Ge Li, H. Noh, A.D. Stone, H. Cao, Time-reversed lasing and interferometric control of absorption, Science 331 (6019) (2011) 889–892.
[11] Stefano Longhi, Coherent perfect absorption in a homogeneously broadened two-level medium, Phys. Rev. 83 (5) (2011), 055804.
[12] K. Ming, Y.D. Chong, H.T. Wang, W. Zhu, M. Premaratne, Critical route for coherent perfect absorption in a Fano resonance plasmonic system, Appl. Phys. Lett. 105 (13) (2014) 1866.
[13] M.B. Pu, M. Wang, C.G. Hu, C. Huang, Z.Y. Zhao, Y.Q. Wang, X.G. Luo, Engineering heavily doped silicon for broadband absorber in the terahertz regime, Opt Express 20 (23) (2012) 25513–25519.
[14] J. Zhang, C. Guo, K. Liu, Z. Zhu, W. Ye, X. Yuan, S. Qin, Coherent perfect absorption and transparency in a nanostructured graphene film, Opt Express 22 (2014) 12524.
[15] J. Zhang, K.F. MacDonald, N.I. Zheludev, Controlling light-with-light without nonlinearity, Light Sci. Appl. 1 (7) (2012) e18.
[16] S. Feng, K. Halterman, Coherent perfect absorption in epsilon-near-zero metamaterials, Phys. Rev. B 86 (16) (2012) pp.165103–1-165103-6.
[17] W. Wan, Y. Chong, L. Ge, H. Noh, A.D. Stone, H. Cao, Time-reversed lasing and interferometric control of absorption, Science 331 (2011) 889–892.
[18] Z.P. Li, S.P. Zhang, N.J. Halas, P. Nordlander, H.X. Xu, Coherent modulation of propagating plasmons in silver-nanowire-based structures, Small 7 (5) (2011) 593–596.
[19] L.N. Pye, M.L. Villinger, S. Shabahang, W.D. Larson, L. Martin, A.F. Abouraddy, Octave-spanning coherent perfect absorption in a thin silicon film, Opt. Lett. 42 (1) (2017) 151–154.
[20] J. Luo, B.B. Liu, Z.H. Hang, Y. Lai, Coherent perfect absorption via photonic doping of zero-index media, Laser Photon. Rev. 20 (Aug. 2018), 1800001, 08.
[21] D.J. Wang, J. Luo, Z.Z. Sun, Y. Lai, Transforming zero-index media into geometry-invariant coherent perfect absorbers via embedded conductive films, Opt Express 29 (4) (2021) 5247–5258.
[22] F.P. Wu, H. Zhang, B.F. Wan, H.F. Zhang, Coherent perfect absorption in the 1-D non-magnetized plasma photonic crystals, Phys. Scripta 96 (12) (2021), 125868.
[23] S.S. Rao, Y.M. Liu, B.F. Wan, H.F. Zhang, Theoretical proposal of a multitasking sensor realized by the mechanism of nonreciprocal absorption evanescent wave in the magnetized ferrite photonic crystals, IEEE Sensor. J. 21 (24) (2021) 27405–27413.
[24] Z.A. Zaky, A.M. Ahmed, A.H. Aly, Refractive index gas sensor based on the Tamm state in a one-dimensional photonic crystal: theoretical optimisation, Sci. Rep. 10 (1) (Jun. 2020) 9736.
[25] B.F. Wan, Y. Xu, Z.W. Zhou, D. Zhang, H.F. Zhang, Theoretical investigation of a sensor based on one-dimensional photonic crystals to measure four physical quantities, IEEE Sensor. J. 21 (3) (2021) 2846–2853.
[26] A. Panda, P.D. Pukhrambam, Design and analysis of 1D photonic crystal doped with magnetized cold plasma defect for application of single/multi-channel tunable narrowband filter, Phys. Scripta 97 (2022), 065507.
[27] Z.A. Zaky, H.A. Amer, B. Suthar, A.H. Aly, Gas sensing applications using magnetized cold plasma multilayers, Opt. Quant. Electron. 54 (4) (2022) 217.

[28] T. Sakaguchi, O. Sakai, K. Tachibana, Photonic bands in two-dimensional microplasma arrays. II. Band gaps observed in millimeter and subterahertz ranges, J. Appl. Phys. 101 (7) (2007).

[29] L.M. Qi, Z.Q. Yang, F. Lan, X. Gao, Z.J. Shi, Properties of obliquely incident electromagnetic wave in 1-D magnetized plasma photonic crystals, Phys. Plasmas 17 (2010), 042501.

[30] W. Zhu, F. Xiao, K. Ming, M. Premaratne, Coherent perfect absorption in an all-dielectric metasurface, Appl. Phys. Lett. 108 (115) (2016), 121901.